Singlet-Triplet Inversion in Triangular Boron Carbon Nitrides

Matteo Bedogni and Francesco Di Maiolo*

Department of Chemistry, Life Science and Environmental Sustainability, Università di Parma, 43124 Parma, Italy.

E-mail: francesco.dimaiolo@unipr.it

Abstract

The discovery of singlet-triplet (ST) inversion in some π-conjugated triangle-shaped boron carbon nitrides is a remarkable breakthrough that defies Hund's first rule. Deeply rooted in strong electron-electron interactions, ST inversion has garnered significant interest due to its potential to revolutionize triplet harvesting in organic LEDs. Using the well-established Pariser-Parr-Pople model for correlated electrons in π-conjugated systems, we employ a combination of CISDT and RASCI calculations to investigate the photophysics of several triangular boron carbon nitrides. Our findings reveal that ST inversion in these systems is primarily driven by a network of alternating electron-donor and electron-acceptor groups in the molecular rim, rather than by the triangular molecular structure itself.

1 Introduction

Hund's first rule places the first excited singlet state S_1 of a closed-shell molecules at a higher energy than the relevant triplet state T_1, resulting in a positive singlet-triplet (ST) gap, ΔE_{ST}. Against this background, recent experimental[1,2] and theoretical[2–17] studies

have demonstrated that various triangle-shaped π-conjugated molecules (also known as triangulenes) adorned with nitrogen atoms exhibit a negative ΔE_{ST}, thereby defying Hund's multiplicity rule. In these systems, the highest occupied molecular orbital (HOMO) and the lowest unoccupied molecular orbital (LUMO) have minimal overlap. As a result, the lowest excited state predominantly exhibits a multi-resonant charge-transfer (MR-CT) character, with the electronic charge transferring from HOMO to LUMO. Under these conditions, the exchange integral, which is responsible for the singlet-triplet (ST) splitting, is very small, and the typically small spin polarization correction can become significant enough to reverse the ST gap.[18–22] Recently, considerable effort has focused on integrating boron and nitrogen atoms into the core of triangulenes to achieve novel photophysical properties.[23–28]

MR-CT chromophores are fascinating for multiple reasons. Even in systems where the singlet and triplet states follow the conventional order, the small ΔE_{ST} allows for thermal population of the S_1 state from the T_1 state.[29–33] Accordingly, MR-CT emitters are being extensively studied as systems showing thermally activated delayed fluorescence (TADF). The exceptionally narrow and minimally solvatochromic emission spectra coming from the dye structural rigidity and reduced polarity of the MR-CT excited state, make them particularly appealing for organic light-emitting diodes (OLED).[1,2,34–45] In this work, we will theoretically investigate the singlet-triplet (ST) inversion in some triangular boron carbon nitrides as efficient molecular structures in electron-transport materials for OLED applications.

Electron correlation lies at the heart of spin-polarization, the phenomenon that underlies ST inversion. Consequently, traditional TD-DFT methods for studying excited states miserably fail in describing singlet-triplet inversion, as was noted early on.[2,46,47] To address ST-inversion, high-quality but computationally demanding methods are typically used, spanning from ADC(2),[2–4,7,8] CC2,[2,3,8,9] EOM-CCSD,[2,4,5,48,49] Mukherjee's multireference coupled- cluster with noniterative triple excitations (Mk-MRCCSD(T)),[50] CC3,[51] Green's functions methods,[10] CIS(D),[3,6] SA-CASSCF,[3,8,50] and NEVPT2.[3,4,8,50]

We adopt a different strategy and conduct an extensive study of various triangular boron

carbon nitrides using the Pariser-Parr-Pople (PPP) model Hamiltonian to account for correlated electrons in π-conjugated molecules. The model dates back to the 1950s,[52–54] and was able to effectively describe ground state as well as excited state properties of several small organic molecules.[53,55–64] The PPP model has recently made a comeback to address ST-inversion in MR-CT dyes for OLED applications. In particular, Jorner *et al.*[13] used the PPP model with configuration interaction singles (CIS) and perturbative double excitations for ultra-efficient virtual screening of possible molecules featuring a negative ΔE_{ST}. In the same period, relying on the PPP model, Bedogni *et al.*[11] showed that triple excitations are needed to properly deal with ST inversion.

In this work, we use the PPP model to investigate ST inversion in 3T triangulenes differently decorated with boron and nitrogen atoms. Indeed, ab initio all-electron triple-CI methods are computationally expensive, making their use prohibitive for such systems. Accordingly, we evaluate the effectiveness of the double configuration interaction and similar second order methods typically used for all-electron models of triangular boron carbon nitrides. Although the PPP model may not yield quantitatively precise results for specific molecules,[13,65] its power lies in the ability to unveil qualitative trends regarding the effects of electron-electron interaction in π-conjugated molecules. The new understanding gained from this analysis adds to what was reported in Ref. 11 on smaller triangulenes, helping to define novel strategies in the quest for molecular systems with small and possibly negative ST gap.

2 Setting-Up the Stage: The Pariser-Parr-Pople Model

The PPP model is the simplest model for correlated electrons in π-conjugated molecules. Similarly to the Hückel model, PPP only accounts for the $2p_z$ atomic orbitals (AO) perpendicular to the molecular plane at each atom position. However, unlike the Hückel model, the PPP model also incorporates electron-electron (e-e) interactions under the zero differential

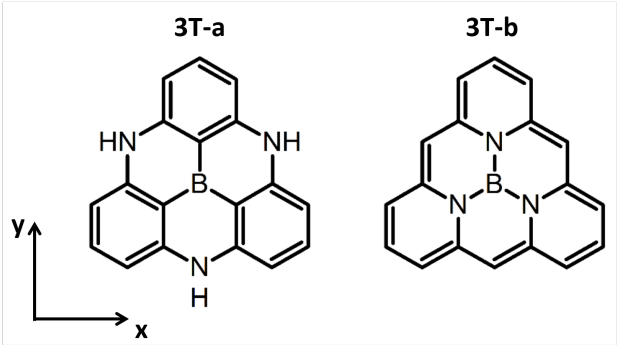

Figure 1: Sketches of the molecular structures of two prototypical 3T systems, trihydrotriazaboradibenzopyrene (shortly, 3T-a) and triazaboradibenzopyrene (shortly, 3T-b).

overlap (ZDO) approximation, thus neglecting overlap integrals for p orbitals on different atomic sites. The PPP model Hamiltonian on the AO basis reads:

$$\begin{aligned}\hat{H}_{PPP} &= \sum_{\mu}\varepsilon_{\mu}\hat{n}_{\mu} - \sum_{\mu\nu,\nu>\mu}\sum_{\sigma} t_{\mu\nu}\left(\hat{a}^{\dagger}_{\mu\sigma}\hat{a}_{\nu\sigma} + \hat{a}^{\dagger}_{\nu\sigma}\hat{a}_{\mu\sigma}\right) \\ &+ \sum_{\mu} U_{\mu}\hat{n}_{\mu\uparrow}\hat{n}_{\mu\downarrow} + \sum_{\mu\nu,\nu>\mu} V_{\mu\nu}\left(Z_{\mu} - \hat{n}_{\mu}\right)\left(Z_{\nu} - \hat{n}_{\nu}\right) \qquad (1)\end{aligned}$$

where $\hat{a}_{\mu,\sigma}$ ($\hat{a}^{\dagger}_{\mu,\sigma}$) annihilates (creates) an electron with spin σ on site μ, and $\hat{n}_{\mu} = \sum_{\sigma}\hat{a}^{\dagger}_{\mu\sigma}\hat{a}_{\mu\sigma}$ counts the total number of electrons on the μ atom. The parameters entering the first line of the above Hamiltonian are defined as follows: ε_{μ} is the on-site orbital energy, while $t_{\mu\nu}$ the hopping amplitude between atomic sites μ and ν. In particular, in the PPP model, hopping occurs only between atoms connected by a σ-bond. The second line of the Hamiltonian accounts for electron-electron interactions: U_{μ} represents the repulsion between two electrons on the μ atom, $V_{\mu\nu}$ denotes the repulsion between electrons on different atoms, while Z_{μ} is the charge on site μ when π-electrons are removed ($Z_{\mu} = 0$ for boron atoms, $Z_{\mu} = 1$ for carbon and aza nitrogen atoms, $Z_{\mu} = 2$ for pyrrole nitrogens). We follow the $V_{\mu\nu}$ expression given by Ohno:[58,61,66]

$$V_{\mu\nu} = \frac{e^2}{4\pi\varepsilon_0}\left[r^2_{\mu\nu} + \left(\frac{\varepsilon_r e^2}{4\pi\varepsilon_0(U_{\mu}+U_{\nu})}\right)^2\right]^{-1/2} \qquad (2)$$

where the relative dielectric constant ε_r is set equal to 2 to account for a typical organic medium.[61]

In the real space (RS) picture, the PPP Hamiltonian is written on the basis that includes all possible states generated by distributing the n π-electrons across the N atoms. In particular, the basis states are chosen as eigenstates of the z-component spin operator $\hat{S}_z$. Accordingly, triplet states can be identified by diagonalizing the PPP Hamiltonian in both $S_z = 0$ and $S_z = 1$ subspaces, looking for those states that are present in both subspaces. As N increases, the size of the RS basis expands rapidly, reaching $\sim$ 420 billion states in the $S_z = 0$ subspace of 3T-a and 3T-b molecules in Fig. 1 (see Supporting Information (SI) Section S2). To make the problem numerically tractable, we rewrite the PPP Hamiltonian in the molecular orbital (MO) picture by introducing $\hat{b}^{(\dagger)}_{k\sigma} = \sum_\mu c_{\mu,k} \hat{a}^{(\dagger)}_{\mu\sigma}$ that annihilates (creates) an electron with spin σ in the k-th MO, and where $c_{k\mu}$ are the expansion coefficients of the k-th MO on the AOs obtained upon diagonalization of the relvant Fock operator (see SI Section S1). With this transformation, the PPP model Hamiltonian in Eq. 1 becomes:[59]

$$
\begin{aligned}
\hat{H}^{CI}_{PPP} &= \sum_{ij}\sum_{\sigma}\left(\sum_{\mu}\varepsilon_\mu c_{\mu,i}c_{\mu,j}\right)\hat{b}^\dagger_{i\sigma}\hat{b}_{j\sigma} \\
&- \sum_{ij}\sum_{\sigma}\left[\sum_{\mu\nu,\mu\neq\nu} t_{\mu\nu}\left(c_{\mu,i}c_{\nu,j} + c_{\nu,i}c_{\mu,j}\right)\right]\hat{b}^\dagger_{i\sigma}\hat{b}_{j\sigma} \\
&+ \sum_{ijkl}\left(\sum_{\mu} U_\mu c_{\mu,i}c_{\mu,j}c_{\mu,k}c_{\mu,l}\right)\hat{b}^\dagger_{i\uparrow}\hat{b}_{j\uparrow}\hat{b}^\dagger_{k\downarrow}\hat{b}_{l\downarrow} \\
&+ \sum_{ijkl}\sum_{\sigma\sigma'}\left(\sum_{\mu,\nu,\mu\neq\nu}\frac{V_{\mu\nu}}{2}c_{\mu,i}c_{\mu,j}c_{\nu,k}c_{\nu,l}\right)\hat{b}^\dagger_{i\sigma}\hat{b}_{j\sigma}\hat{b}^\dagger_{k\sigma'}\hat{b}_{l\sigma'} \\
&- \sum_{ij}\sum_{\sigma}\left[\sum_{\mu,\nu,\mu\neq\nu}\frac{V_{\mu\nu}}{2}\left(Z_\nu c_{\mu,i}c_{\mu,j} + Z_\mu c_{\nu,i}c_{\nu,j}\right)\right]\hat{b}^\dagger_{i\sigma}\hat{b}_{j\sigma}
\end{aligned}
\tag{3}
$$

where i, j, k and l run on the molecular orbitals, while μ and ν run on the atomic sites. The above Hamiltonian is written on the basis defined by the ground state configuration and the single, double, triple, etc. excited configurations obtained by promoting one, two, three,

etc. electrons from the occupied to the virtual MOs. The resulting matrix is attacked by using efficient algorithms designed for storing and diagonalizing large matrices.[67] The PPP Hamiltonian in Eq. 3 is much less sparse than on the RS basis. Nonetheless, as showed in Ref. 11 for 2T triangulenes, results rapidly converge with the number of CI excitations, making it possible to reliably attack excited state properties of 3T triangulenes. Furthermore, in order to handle electron correlation more efficiently, we compared CI results with those obtained by strategically partitioning the PPP MOs into different active spaces, adopting a Restricted Active Space Configuration Interaction (RASCI) approach.[68,69] Following the commonly used RASCI scheme, we divided the PPP HF-MOs into three distinct subspaces: RAS1, RAS2, and RAS3, arranged in order of increasing orbital energy. RAS1 consists of occupied orbitals, RAS2 of occupied and virtual MOs, while RAS3 of virtual orbitals. The simplest RASCI approach includes all possible excitations within the RAS2 space, thus leading to a *reduced full-CI* called complete active space CI (CASCI). To improve on this, the hole-particle approximation can be applied, allowing a fixed number of excitations out of RAS1 (electron vacancies or holes in RAS1) and a fixed number of electrons (particles) in RAS3. This creates a hierarchy of methods that progressively increase the correlation captured in the RASCI solution. For instance, allowing only one excitation either out of RAS1 into RAS2 or from RAS2 into RAS3 results in RASCI(h,p).[70] Further refinement is achieved with RASCI(h,p,hp), where single excitations from RAS1 into RAS3 are also considered. Of course, RASCI results are highly sensitive to the distribution of MOs and electrons among RAS1, RAS2, and RAS3. However, as demonstrated below, when the RAS2 space includes 4 electrons distributed across 6 MOs, the RASCI(h,p,hp) results for 3T-a and 3T-b converge to those obtained at the CISDT theory level, but with a significantly reduced computational cost (see SI section S2).

Molecular excited states $|f\rangle$ obtained from the diagonalization of the CI Hamiltonian are

used for calculating optical spectra. The relvant electric dipole moment operator reads:

$$\hat{\vec{\mu}} = \hat{\mu}_x \vec{i} + \hat{\mu}_y \vec{j} = \sum_{ij} \sum_{\sigma} \left[\sum_{\mu} \left(Z_\mu \delta_{ij} - c_{\mu i} c_{\mu j} \right) \left(x_\mu \vec{i} + y_\mu \vec{j} \right) \right] \hat{b}^\dagger_{i\sigma} \hat{b}_{j\sigma} \tag{4}$$

where δ_{ij} is the Kronecker delta, x_μ, y_μ are the Cartesian coordinates of site μ in the molecular plane. Consequently, absorption spectra are calculated as:

$$A(\omega) \quad \propto \quad \omega \sum_f |\mu_{fg}|^2 \exp \left[\frac{(\omega - \omega_{fg})^2}{2\sigma^2} \right] \tag{5}$$

where the sum runs over the excited eigenstates, $\omega_{fg} = E_f - E_g$ and $\mu_{fg} = \langle f|\hat{\mu}|g\rangle$ being the relevant transition energies and transition dipole moments, respectively, and where we assigned a Gaussian bandshape to each transition (in the following $\sigma = 0.1$ eV).

3 Results and discussion

3.1 3T-a and 3T-b as Benchmark Systems

Modeling triangular boron carbon nitrides presents challenges, particularly due to the scarcity of experimental spectroscopic data. In this study, we start focusing on the two 3T boron-centered triangulenes shown in Fig. 1. Although 3T-a is not expected to violate Hund's multiplicity rule,[25] experimental absorption spectra are available and can be used to parameterize and validate the PPP model. Conversely, 3T-b is expected to exhibit a negative ΔE_{ST},[71] but, to the best of our knowledge, no experimental spectroscopic data exist for it. The PPP parameters for carbon atoms date back the 1950s,[53] are well-defined and transferable across different molecules.[58,61,72,73] For carbons, we set the on-site energy to zero, use a standard on-site electron-electron interaction value of $U_C = 11.26$ eV, and a nearest-neighbor C-C hopping value of $t = -2.4$ eV. For pyrrole nitrogen atoms, there is no single set of PPP parameters that is universally accepted.[57–61,72,74–80] Accordingly, we used the PPP

parameters we identified for the nitrogen-centered 2T triangulenes in Ref. 11, setting the on-site electron-electron repulsion at $U_N = 15$ eV and the site energy ε_N^{py} at -13 eV. Similarly, multiple sets of PPP parameters exist for boron atoms.[81–87] We fixed the boron on-site Coulombic repulsion at $U_B = 10$ eV and fine-tuned the boron site-energy ε_B to best match the experimental spectra of 3T-a. The hopping integrals for B-N, B-C, and C-N bonds were set equal to that for C-C bonds, a choice that has a minimal impact on the results (see SI Section S3). For the molecular geometry, we set all angles to 120° and all bond lengths to 1.4 Å. Results for different geometries are marginally different, as detailed in the SI Section S3.

The experimental absorption spectrum of 3T-a, as reported in Ref. 25, is depicted by the red line in the inset of Fig. 2b, showing a sharp transition around 3.2 eV. Conversely, no experimental data is available for 3T-b. Panels b and e of the same figure display spectra calculated at the PPP-RASCI(h,p,hp) theory level, with the RAS2 subspace encompassing 4 electrons and the 6 MOs shown in panels a and d, respectively, providing converged results and computational accuracy (as detailed below). We present these results across a range of on-site energy values for the central boron, ε_B, spanning from 7 eV to 14 eV. The lowest dark singlet state, characterized by A_2' symmetry in the D_{3h} molecular point group, is indicated by a cross in panels b and e.

For 3T-a (Fig. 2b), as the electron-donating nature of the central boron increases (i.e., with more positive ε_B), both the highest energy excitation and the band corresponding to the first doubly degenerate E' state undergo a blueshift. In contrast, the dark state shifts to the red, but still stays above the bright E' state. Agreement with experimental data is observed within the range of 10 eV $< \varepsilon_B <$ 12 eV. Within this range, the ST gap remains positive (see the gray shaded area in panel c), consistent with the observations in Ref. 25.

For 3T-b (Fig. 2e), as ε_B becomes more positive, the dark state shifts to the red, while the bright states shift to the blue. Unlike 3T-a, for $\varepsilon_B \geq 9$ eV, the first bright E' state is positioned above the A_2' dark state. Within the range of ε_B from 10 eV to 12 eV (highlighted

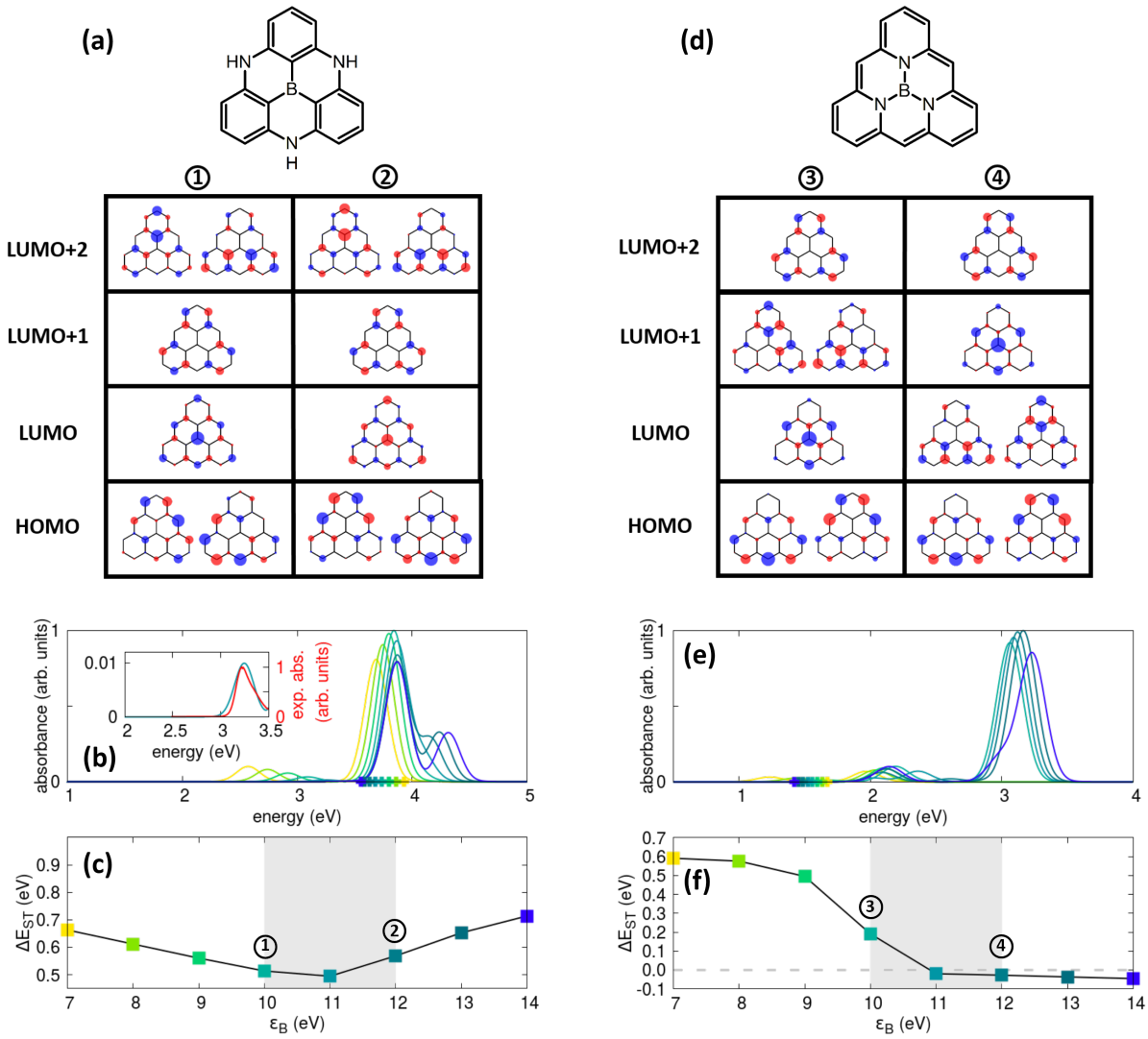

Figure 2: Simulating the photophysics of 3T-a (panels a-c) and 3T-b (panels d-f). (a) 3T-a frontier MOs entering RAS2 subspace, for two values of ε_B; (b) Absorption spectra of 3T-a: colored lines show results for several ε_B values (same color code as in panel c), the crosses mark the position of the first dark singlet excited state. Calculated spectra are normalized to the maximum absorbance of the most intense spectrum. The inset shows the comparison between the experimental spectrum (red curve) from Ref. 25 and the spectrum calculated for $\varepsilon_B = 11$ eV; (c) 3T-a singlet-triplet energy gaps calculated for different ε_B values, the gray shaded area highlights ε_B values giving acceptable agreement between calculated and experimental absorption spectra. (d) The same as (a) for 3T-b; (e) Absorption spectra of 3T-b: colored lines show results for several ε_B values (same color code as in panel f), the crosses in the low energy region mark the position of the first dark singlet excited state. Calculated spectra are normalized to the maximum absorbance of the most intense spectrum. (f) The same as (c) for 3T-b.

in gray in panel e), the ST gap of 3T-b transitions from positive, $\Delta E_{ST} = 0.6$ eV at $\varepsilon_B = 7$ eV, to negative, $\Delta E_{ST} = -0.05$ eV at $\varepsilon_B = 14$ eV. Consequently, $\varepsilon_B = 11$ eV is chosen as an optimal compromise to describe both the experimental absorption spectrum of 3T-a and the negative ΔE_{ST} of 3T-b. Unless otherwise stated, subsequent results will use this ε_B value.

The Hartree-Fock molecular orbitals of 3T-a and 3T-b, depicted in Fig. 2a and d, respectively, offer valuable insights. Both molecules show a doubly degenerate HOMO within the ε_B range considered. For 3T-a, the LUMO is never complementary to the HOMO, resulting in a positive ST gap across the entire ε_B range. In the case of 3T-b, a positive ST gap (point ③ in panel f) corresponds to a lack of HOMO-LUMO complementarity. However, when the ST gap turns negative (point ④ in Fig. 2f), the LUMO and LUMO+1 roles are reversed, making the LUMO doubly degenerate and achieving HOMO-LUMO complementarity.

The varying ΔE_{ST} behavior observed for 3T-b with changes in the boron site energy underscores the crucial role of the triangulene's central atom. Figure 3 illustrates the ST gap dependence on the triangulene center parameters, specifically ε_B and U_B. The green dot represents the optimal boron parameters identified in Fig. 2, i.e., $U_B = 10$ eV and $\varepsilon_B = 11$ eV. Starting from this position, reducing the central atom on-site electron-electron repulsion below ∼8 eV results in the loss of ST inversion. Conversely, increasing the boron atom's on-site energy ε_B favors ST inversion.

As shown, 3T-b is positioned on the edge of the ST inverted region (green dot on the map) with a slightly negative ST gap of -0.03 eV. This observation contrasts somewhat with ADC(2) results from Ref. 71, which predict a more pronounced ST inversion with $\Delta E_{ST} = -0.28$ eV. The PPP model, while not exact, provides results influenced by the chosen molecular geometry and model parameters (see SI Section S3). However, it is important to acknowledge that widely used all-electron approaches come with inherent approximations. Specifically, ADC(2) estimates show significant uncertainties in $\pi \rightarrow \pi^*$ transition energies, with errors of about 0.22 eV for low-lying singlet states and approximately 0.12 eV for low-lying triplet states,[88] resulting in an error in ΔE_{ST} that is comparable to the calculated gap.

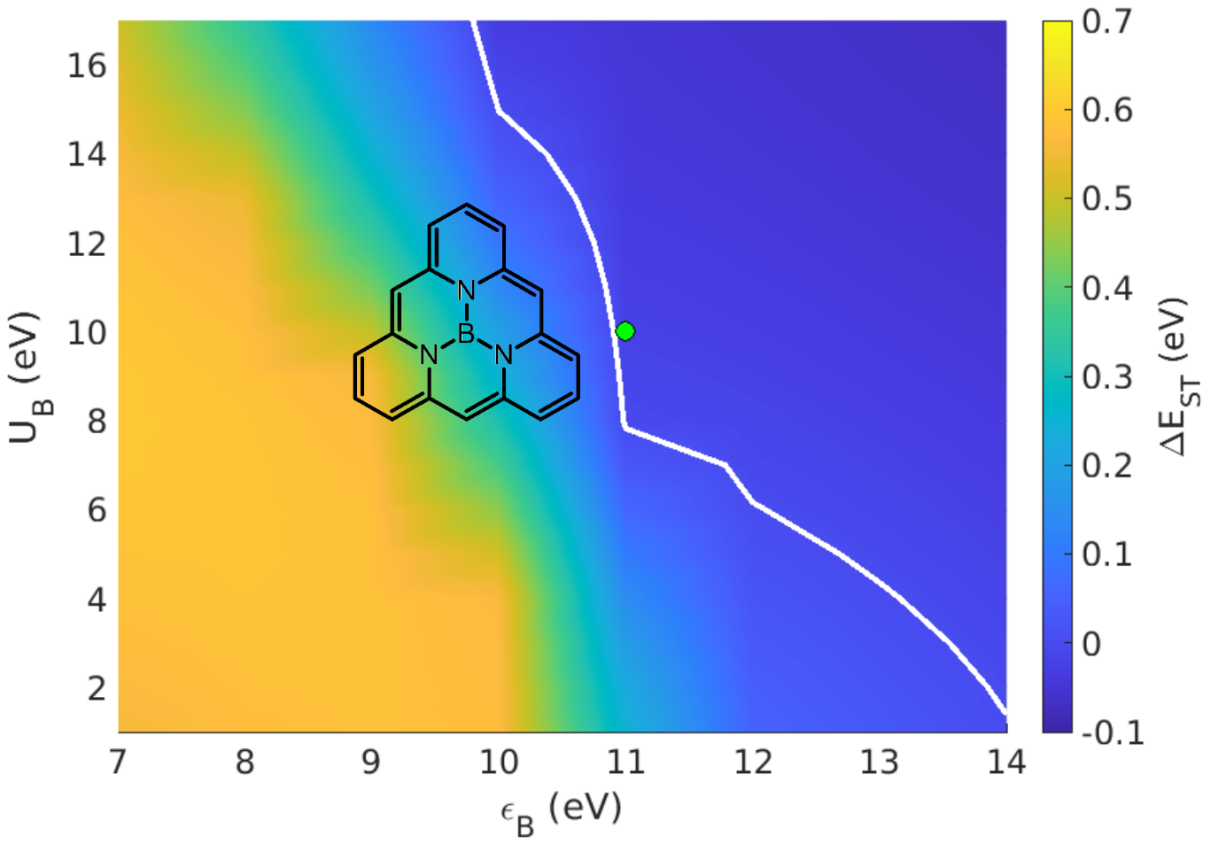

Figure 3: The color map illustrates how the ST gap in 3T-b varies with U_B and ε_B. The white curve at $\Delta E_{ST} = 0$ defines the boundary between the ST inverted region (dark blue) and the normal region (light blue and yellow). The green dot represents the values $U_B = 10$ eV and $\varepsilon_B = 11$ eV pertinent to 3T-b. Calculations performed at the PPP-RASCI(h,p,hp) level, using the model parameters specified in the main text.

Acceptable errors are achieved with third-order techniques, such as CC3, which has a mean absolute error of 0.02 eV for $\pi \rightarrow \pi^*$ transitions.[89] However, these methods are prohibitively expensive for systems as large as the 3T triangulenes discussed in this work.

This allows us to assess the reliability of widely used all-electron calculations while validating our approach. For 3T triangulenes, typically used all-electron methods include CIS with perturbative double excitations (i.e., CIS(D)), equation-of-motion coupled-cluster singles and doubles (EOM-CCSD), similarity transformed EOM domain-based local pair natural orbital CCSD (STEOM-DLPNO-CCSD),[15] and second-order algebraic diagrammatic construction (ADC(2)).[71] These approaches highlight the critical role of double excitations in

accurately describing ST inversion. Additionally, Ref. 11 demonstrates that triple excitations are necessary for a precise treatment of singlet-triplet inversion. However, the rapid increase in the number of multiple excited configurations makes third-order studies using all-electron methods impractical for large systems. Conversely, the PPP model, with its minimal representation of π-electrons, is exceptionally well-suited for exploring the significance of higher-order excited configurations in systems as large as 3T triangulenes.

In Fig. 4a and b, we illustrate the relative contributions of single (S), double (D), and triple (T) excitations in the lowest seven eigenstates of 3T-a and 3T-b. For both molecules, singly and triply excited configurations have minimal contribution to the ground state. In line with Brillouin's theorem, single and triple CIs do not directly mix with the ground state configuration and only contribute marginally through indirect interactions with doubly excited configurations. In the excited states, both molecules show double and triple excitations contributing similarly, around 10%. This finding aligns with our results for 2T triangulenes in Ref. 11 and indicates that a reliable approach to the excited states of these molecules should include not oly double, but also triply excited configurations.

Panels c and d reveal that truncating the expansion at the CISD level stabilizes the ground state, but the stabilization of the excited states due to triple excitations is missing. As a result, CISD overestimates transition energies, an error corrected when triply excited configurations are included. However, achieving triple-CI in all-electron quantum chemical calculations is prohibitively expensive and impractical for systems as large as 3T triangulenes. Most often, CIS(D) approaches, where double CIs are introduced perturbatively, provide reasonable transition energies.[15] Nevertheless, caution is needed because in CIS(D) the perturbative correction from double-CIs only affects the energies, leaving the wavefunctions at the CIS level, thus impacting the accuracy of the calculated transition dipole moments.

Furthermore, panels c and d also reveal an interesting trend. In 3T-b, the A_2' excited singlet state and E' excited triplet state have a normal order (positive ST gap) at the CIS

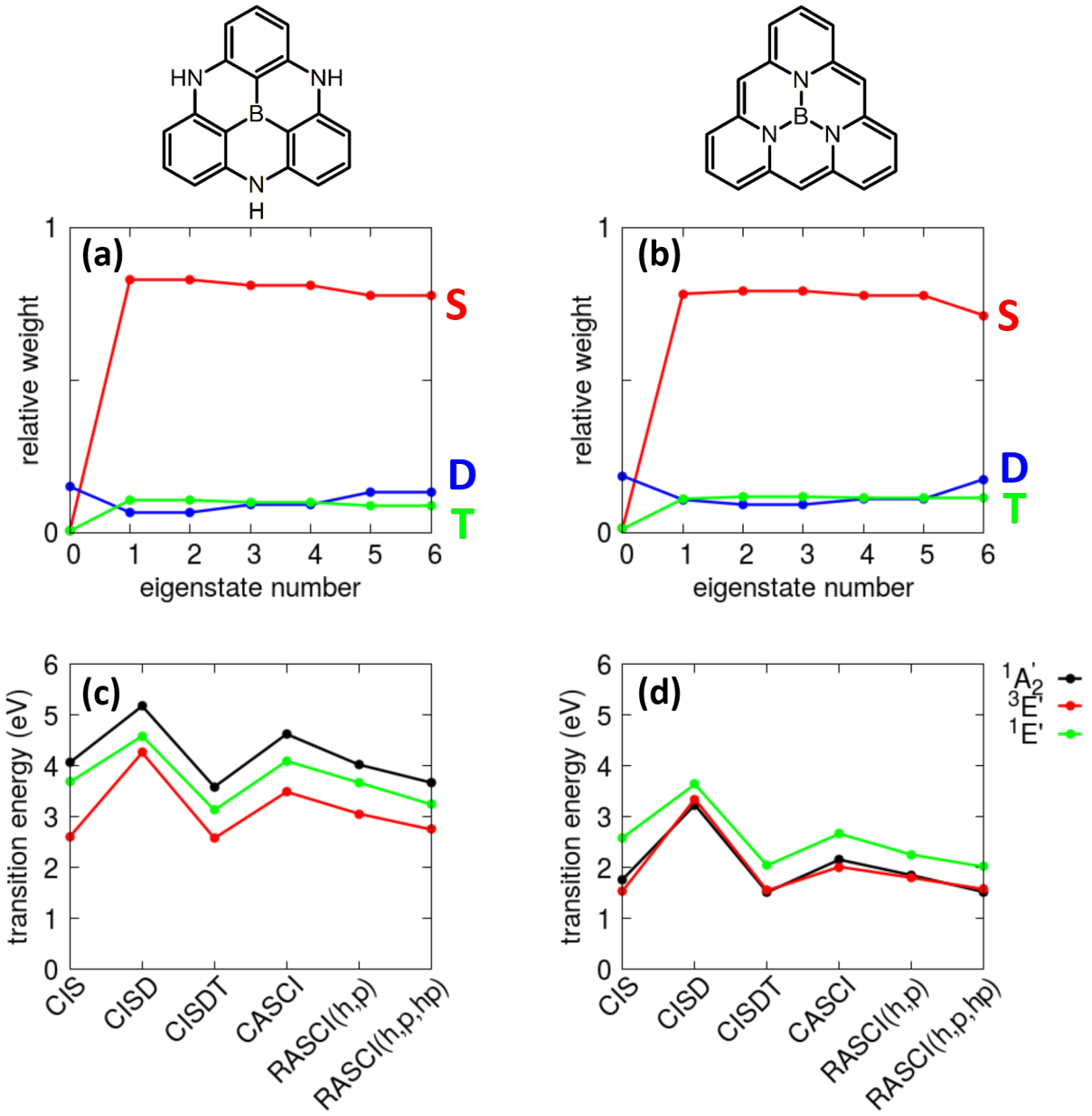

Figure 4: Relative contributions of singly (S), doubly (D), and triply (T) excited configurations for the first seven singlet and triplet eigenstates of 3T-a (panel a) and 3T-b (panel b) calculated at the PPP-CISDT level, along with the excitation energies of the first few electronic states of 3T-a (panel c) and 3T-b (panel d) at various theoretical levels. Model parameters are specified in the main text.

level, but as correlations are included (from CISD onward), their order inverts, with the triplet state lying higher than the dark singlet. The bright E' singlet state consistently remains above the E' triplet state. In contrast, in 3T-a, the A_2' singlet is always well above

both the E' triplet and E' singlet excited states, with no ST inversion observed.

To enhance computational efficiency, we compared PPP-CI results with those obtained at the PPP-RASCI level, which eliminates potentially negligible high-energy configurations by restricting the number of holes/particles in the lower and higher HF-MOs. This limitation reduces the overall number of configurations, making RASCI more computationally efficient than CISDT. We started by selecting a subset of MOs to span the active RAS2 space, where all possible electron excitations are considered (reduced full-CI or CASCI). This active space should include the most chemically relevant MOs for the system. For 3T triangulenes, we used a RAS2 subspace containing the doubly degenerate HOMO and the next 4 virtual molecular orbitals, totaling 4 electrons in 6 MOs (see Fig. 2a and d).

Panels c and d show that CASCI systematically overestimates transition energies by approximately 1 eV for 3T-a and 0.6 eV for 3T-b. Furthermore, in 3T-b, the ST inversion is lost, resulting in a positive ST gap of +0.15 eV. To improve on CASCI results, we used the RASCI hole and particle approach, accounting for additional excitations involving the remaining molecular orbitals spanning RAS1 and RAS3. Specifically, in RASCI(h,p), we included single excitations from RAS1 to RAS2 and from RAS2 to RAS3, bringing transition energies closer to those calculated at CISDT level. When we also accounted for single excitations from molecular orbitals in RAS1 directly to RAS3 (i.e., RASCI(h,p,hp)), the results converged to the CISDT ones, recovering the negative ΔE_{ST} for 3T-b. This is particularly noteworthy because RASCI(h,p,hp) used only 48,705 states out of the 786,181 states in the CISDT calculation, significantly reducing computational time and memory usage (see SI Section S2). Given its balance between computational cost and accuracy, RASCI(h,p,hp) was employed for the exploratory studies in this work.

3.2 ST Inversion: The Effect of the Triangulene Rim

In Ref. 11, it was shown that the rim of 2T triangulene is essential for achieving a negative ST gap, requiring an alternating pattern of electron donor and acceptor units. In 3T-b, with

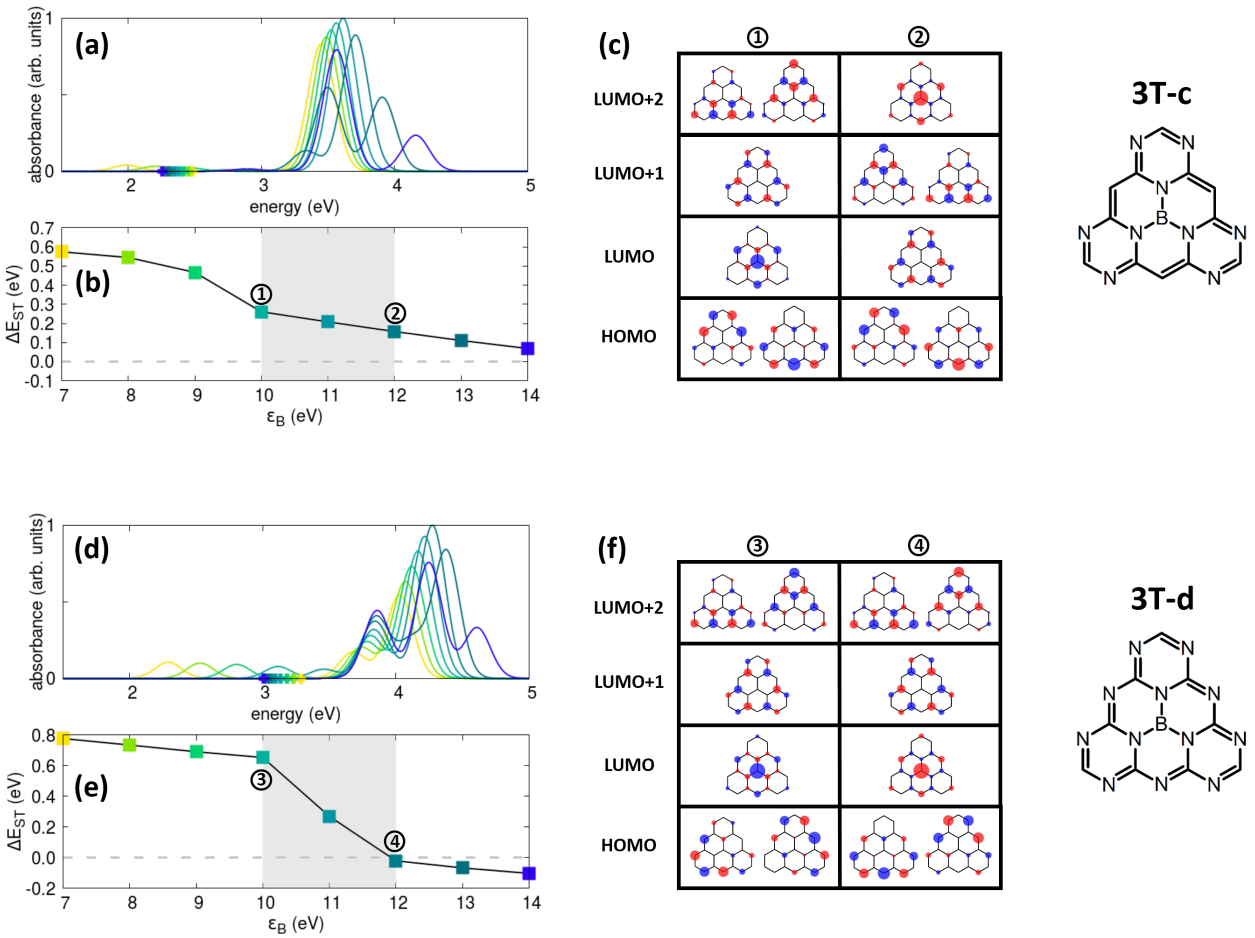

Figure 5: Decorating the rim of 3T-b with an increasing number of aza nitrogens while varying the boron site energy. The calculated absorption spectra (panels a and d), ST gap (panels b and e), and HF frontier orbitals (panels c and f) are presented for nonaazaboradibenzopyrene (shortly, 3T-c) and dodecaazaboradibenzopyrene (shortly, 3T-d). In panels a and d, spectra are normalized to the maximum absorbance of the most intense spectrum. The gray shaded area in panels b and e indicates the region where ε_B takes realistic values as found in Fig. 2. Other parameters are defined in the main text. Calculations performed at the PPP-RASCI(h,p,hp) theory level.

its rim composed of 18 carbon atoms, the central borazinic BN_3 core creates a pattern of electron-rich and electron-poor sites on the rim, resulting in a negative ST gap for $\varepsilon_B \geq 11$ eV. To further investigate the rim role in 3T triangulenes, we decorated the external edge of 3T-b with varying numbers of aza nitrogen atoms, as shown in Fig. 5. Following Ref. 11, we set the site energy of the aza nitrogen at $\varepsilon_N^{aza} = -5$ eV and the on-site electron-electron interaction at $U_N^{aza} = 15.5$ eV.

Compared to Fig. 2 panel e, as relevant to 3T-b, all spectral features shift to the blue as the number of N atoms on the external rim increases (see Fig. 5 panels a and d). Conversely, the dark A_2' singlet state shifts to the red as ε_B becomes more positive. Interestingly, as shown in panel b, the ST gap of 3T-c remains positive throughout the entire ε_B range considered. If the central boron atom is destabilized, making ε_B more positive, the LUMO nature changes, with most of its amplitude shifting from the central boron to the molecular rim (as seen when moving from point ① to point ②). In both cases, the HOMO and LUMO exhibit minimal overlap (see panel c), diminishing the multiresonant character of the dark A_2' singlet state. For 3T-d, no changes in the HOMO and LUMO characteristics are observed while increasing ε_B, and despite the lack of complementarity between the HOMO and LUMO across the entire ε_B range (see panel f), ST inversion occurs for $\varepsilon_B \geq 12$ eV (see panel e).

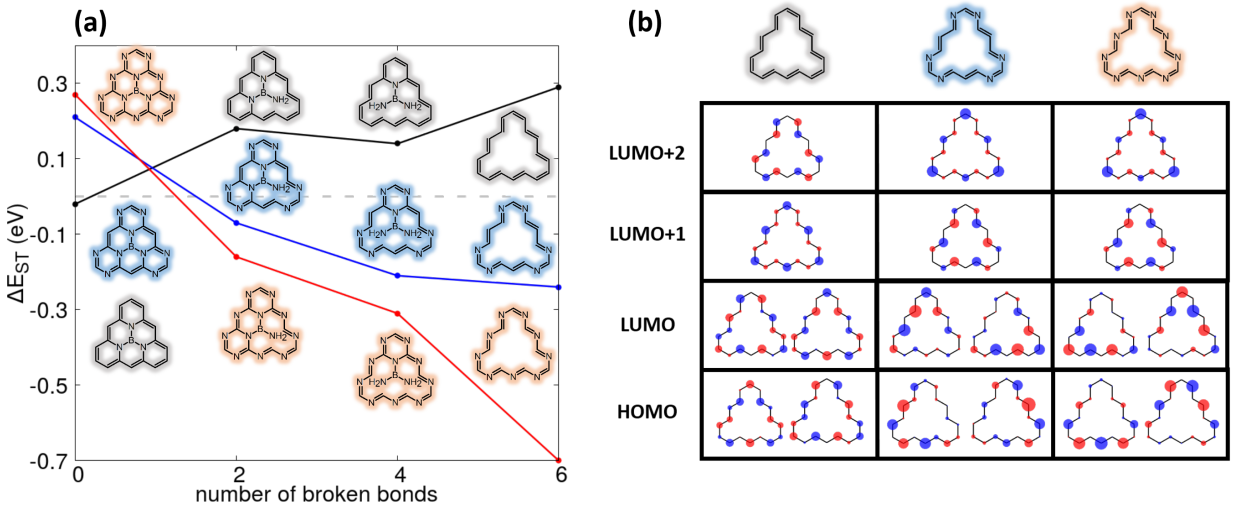

Figure 6: The impact of core connectivity on the ST gap. Panel a: Calculated ST gap as a function of the number of broken central bonds for 3T-b (black curve), 3T-c (blue curve), and 3T-d (red curve). Calculations performed at the PPP-RASCI(h,p,hp) theory level. Panel b: Frontier HF molecular orbitals for the three annulenes obtained by breaking all six bonds connecting the BN_3 core to the triangulene rim in 3T-b, 3T-c, and 3T-d. Same model parameters as in Fig. 4.

To further investigate the role played by the molecular edge in 3T-b, 3T-c, and 3T-d, we broke some of the bonds connecting the borazine BN_3 core to the molecular edge, as shown in Fig. 6. Interestingly, in 3T-b, breaking these bonds quickly shifts the molecule from an

inverted ST order to a normal region, while the opposite effect is observed for 3T-c and 3T-d. As expected, when two or four central bonds are broken and the system symmetry is reduced, the lowest-lying singlet state gains significant oscillator strength. However, breaking all six bonds connecting the borazine core to the triangulene rim restores D_{3h} symmetry, making the lowest energy singlet state optically forbidden (see SI Section S4).

In 3T-c, the ST gap becomes as negative as -0.24 eV, while in 3T-d, without the central borazine core, the ST gap reaches a substantial negative value of -0.7 eV. This implies that the triangulene structure itself is not required to observe ST inversion, as also demonstrated with smaller 2T triangulenes in Ref. 11. Furthemore, if we think to the two starting dyes, 3T-a and 3T-b in Fig. 2, it is evident that ST inversion is favored when pyrrole nitrogen atoms are directly connected to the central boron atom and the on-site energy of the central boron is more positive.

Fig. 6 panel b shows the frontier HF molecular orbitals calculated for cyclooctadecanonaene ($C_{18}H_{18}$), hexaazacyclooctadecanonaene ($C_{12}N_6H_{12}$), and nonaazacyclooctadecanonaene ($C_9N_9H_9$) molecules, corresponding to the rims of the 3T-b, 3T-c, and 3T-d molecules. In $C_{18}H_{18}$, the absence of spatial separation between the HOMO and LUMO leads to a positive ST gap of 0.29 eV. In contrast, the frontier orbitals of $C_{12}N_6H_{12}$ and $C_9N_9H_9$ exhibit their multiresonant nature, resulting in significantly negative ΔE_{ST} values.

4 Conclusions

Singlet-triplet inversion is an intriguing phenomenon in molecular photophysics that defies Hund's multiplicity rule. Exchange interactions typically cause triplet states to have lower energy than the corresponding singlet states. To achieve singlet-triplet inversion, one must minimize the HOMO-LUMO exchange interaction, and a potential strategy for this is to design molecules with negligible HOMO-LUMO overlap. This characteristic is found in multiresonant charge-transfer dyes, a class of π-conjugated molecules where the spatial

separation of HOMO and LUMO facilitates ST inversion. Once the exchange energy is minimized, spin polarization can effectively lower the energy of the lowest excited singlet below that of the lowest triplet. Spin polarization originates from electron correlations and cannot be accurately modeled by considering only singly excited configurations. Consequently, TD-DFT is unsuitable for describing ST inversion and a plethora of post Hartree-Fock approaches are typically used. However, due to their high computational cost, these methods are poorly suited to being used for exploratory studies. Therefore, it is logical to resort to the PPP model, the simplest framework that enables the description of interacting electrons in π-conjugated systems. Due to its simplicity, the PPP model is also well-suited for studying the impact of higher-order excited configurations in ST inversion.

Using the PPP model, we conducted an exploratory study on ST inversion in 3T triangular boron carbon nitrides. We began by validating the model on two prototypical 3T boron-centered triangulenes, 3T-a and 3T-b (cf. Fig. 1). With realistic parameter values, we identified a significant portion of the parameter space for 3T-b (but not for 3T-a) that features a negative ST gap (cf. Figs. 2 and 3).

In Fig. 4, we demonstrated that triply excited configurations contribute significantly and are necessary for accurately addressing ST inversion. However, including triple excitations in systems as large as 3T triangulenes is computationally very demanding even for PPP (as shown in Table 1S), making their use in exploratory studies prohibitive. The PPP-RASCI approach, combined with the hole/particle approximation, represents an excellent compromise between computational efficiency and accuracy. By defining a reduced active space RAS2 containing 4 electrons and 6 molecular orbitals, one can achieve convergence to CISDT results by considering a reduced number of single excitations involving RAS1 and RAS3 subspaces.

The key ingredient for a negative singlet-triplet gap is a molecular edge with alternating electron-donor (D) and electron-acceptor (A) groups. In 3T-b, where the rim is made of 18 carbon atoms, the central borazine unit plays a fundamental role creating an alternating

pattern of electron poor and electron rich sites on the rim, thus leading to a negative ST gap. Accordingly, upon gradually breaking the bonds that connect the central BN_3 unit to the edge, one recovers a cyclic polyene structure, losing the ST inversion (see Fig. 6).

Furthermore, by decorating the edge of 3T-b with six and nine nitrogen atoms we obtained 3T-c and 3T-d (see Fig. 5). Here, the aza nitrogens along the rim create by themselves an alternating electron donor-electron acceptor pattern and the borazine core is not actually needed to observe ST inversion. Rather, in 3T-c and 3T-d the central BN_3 unit is harmful to ST inversion, causing loss of ST inversion for 3T-c and shrinking the inverted ST gap region for 3T-d. (see Fig. 5). Accordingly, in the PPP π-electron only picture, $C_{12}N_6H_{12}$ and $C_9N_9H_9$ rings in an idealized planar geometry are the most promising structures for ST inversion with ST gaps as negative as -0.24 eV and -0.7 eV, respectively.

Data Availability Statement

The data that support the findings of this study are available from the corresponding author upon reasonable request.

Acknowledgement

We thank Prof. Anna Painelli for valuable discussions. We acknowledge financial support from Bando di ateneo per la ricerca 2023 - azione B and from PNRR MUR project ECS-00000033-ECOSISTER. This work benefited from the equipment and framework of the COMP-R Initiative, funded by the *Departments of Excellence* program of the Italian Ministry for University and Research (MUR, 2023-2027) and from the support of the HPC (High Performance Computing) facility at the University of Parma. We acknowledge the CINECA award under the ISCRA initiative, for the availability of high performance computing resources and support (project IsCb8_InveST (HP10CIDH42)). F.D.M. position was co-funded by the European Union - PON Research and Innovation 2014-2020.

Supporting Information Available

Electronic Supplementary Information (SI) available: Sec. S1 contains the PPP model in the Hartree-Fock approximation; Sec. S2 collects information on the basis set dimension and computation timings; Sec. S3 collects additional results obtained for different model parameters values as well as different molecular geometries (i.e., angles and bond lengths); Sec. S4 collects optical spectra calculated for the systems in Fig. 6.

References

(1) Aizawa, N.; Pu, Y.-J.; Harabuchi, Y.; Nihonyanagi, A.; Ibuka, R.; Inuzuka, H.; Dhara, B.; Koyama, Y.; Nakayama, K.-i.; Maeda, S.; Araoka, F.; Miyajima, D. Delayed fluorescence from inverted singlet and triplet excited states. *Nature* **2022**, *609*, 502–506.

(2) Ehrmaier, J.; Rabe, E. J.; Pristash, S. R.; Corp, K. L.; Schlenker, C. W.; Sobolewski, A. L.; Domcke, W. Singlet–triplet inversion in heptazine and in polymeric carbon nitrides. *The Journal of Physical Chemistry A* **2019**, *123*, 8099–8108.

(3) Ricci, G.; San-Fabián, E.; Olivier, Y.; Sancho-García, J. C. Singlet-Triplet Excited-State Inversion in Heptazine and Related Molecules: Assessment of TD-DFT and *ab initio* Methods. *ChemPhysChem* **2021**, *22*, 553–560.

(4) Pollice, R.; Friederich, P.; Lavigne, C.; dos Passos Gomes, G.; Aspuru-Guzik, A. Organic molecules with inverted gaps between first excited singlet and triplet states and appreciable fluorescence rates. *Matter* **2021**, *4*, 1654–1682.

(5) Bhattacharyya, K. Can TDDFT render the electronic excited states ordering of Azine derivative? A closer investigation with DLPNO-STEOM-CCSD. *Chemical Physics Letters* **2021**, *779*, 138827.

(6) Ghosh, S.; Bhattacharyya, K. Origin of the Failure of Density Functional Theories in Predicting Inverted Singlet–Triplet Gaps. *The Journal of Physical Chemistry A* **2022**, *126*, 1378–1385.

(7) Sobolewski, A. L.; Domcke, W. Are heptazine-based organic light-emitting diode chromophores thermally activated delayed fluorescence or inverted singlet–triplet systems? *The Journal of Physical Chemistry Letters* **2021**, *12*, 6852–6860.

(8) Sanz-Rodrigo, J.; Ricci, G.; Olivier, Y.; Sancho-Garcia, J.-C. Negative singlet–triplet excitation energy gap in triangle-shaped molecular emitters for efficient triplet harvesting. *The Journal of Physical Chemistry A* **2021**, *125*, 513–522.

(9) Hall, D.; Sancho-García, J. C.; Pershin, A.; Ricci, G.; Beljonne, D.; Zysman-Colman, E.; Olivier, Y. Modeling of Multiresonant Thermally Activated Delayed Fluorescence EmittersProperly Accounting for Electron Correlation Is Key! *Journal of Chemical Theory and Computation* **2022**, *18*, 4903–4918.

(10) Monino, E.; Loos, P.-F. Connections and performances of Green's function methods for charged and neutral excitations. *The Journal of Chemical Physics* **2023**, *159*.

(11) Bedogni, M.; Giavazzi, D.; Di Maiolo, F.; Painelli, A. Shining Light on Inverted Singlet–Triplet Emitters. *Journal of Chemical Theory and Computation* **2023**, *20*, 902–913.

(12) Omar, H.; Xie, X.; Troisi, A.; Padula, D. Identification of Unknown Inverted Singlet–Triplet Cores by High-Throughput Virtual Screening. *Journal of the American Chemical Society* **2023**, *145*, 19790–19799.

(13) Jorner, K.; Pollice, R.; Lavigne, C.; Aspuru-Guzik, A. Ultrafast Computational Screening of Molecules with Inverted Singlet–Triplet Energy Gaps Using the Pariser–Parr–Pople Semiempirical Quantum Chemistry Method. *The Journal of Physical Chemistry A* **2024**, *128*, 2445–2456.

(14) Barneschi, L.; Rotondi, L.; Padula, D. Molecular Geometry Impact on Deep Learning Predictions of Inverted Singlet–Triplet Gaps. *The Journal of Physical Chemistry A* **2024**, *128*, 2417–2426.

(15) Izu, A. E.; Matxain, J. M.; Casanova, D. Reverse intersystem crossing mechanisms in doped triangulenes. *Physical Chemistry Chemical Physics* **2024**, *26*, 11459–11468.

(16) Majumdar, A.; Ramakrishnan, R. Resilience of Hund's rule in the chemical space of small organic molecules. *Physical Chemistry Chemical Physics* **2024**, *26*, 14505–14513.

(17) Karak, P.; Manna, P.; Banerjee, A.; Ruud, K.; Chakrabarti, S. Reverse Intersystem Crossing Dynamics in Vibronically Modulated Inverted Singlet-Triplet Gap System: A Wigner Phase Space Study. **2024**,

(18) Kollmar, H.; Staemmler, V. A theoretical study of the structure of cyclobutadiene. *Journal of the American Chemical Society* **1977**, *99*, 3583–3587.

(19) Kollmar, H.; Staemmler, V. Violation of Hund's rule by spin polarization in molecules. *Theoretica Chimica Acta* **1978**, *48*, 223–239.

(20) Koseki, S.; Nakajima, T.; Toyota, A. Violation of Hund's multiplicity rule in the electronically excited states of conjugated hydrocarbons. *Canadian Journal of Chemistry* **1985**, *63*, 1572–1579.

(21) Toyota, A.; Nakajima, T. Violation of Hund's multiplicity rule in the lowest excited singlet–triplet pairs of cyclic bicalicene and its higher homologues. *J. Chem. Soc., Perkin Trans. 2* **1986**, 1731–1734.

(22) Toyota, A. Violation of Hund's rule in the lowest excited singlet-triplet pairs of dicyclohepta[cd,gh]pentalene and dicyclopenta[ef,kl]heptalene. *Theoretica Chimica Acta* **1988**, *74*, 209–217.

(23) Hirai, H.; Nakajima, K.; Nakatsuka, S.; Shiren, K.; Ni, J.; Nomura, S.; Ikuta, T.; Hatakeyama, T. One-Step Borylation of 1,3-Diaryloxybenzenes Towards Efficient Materials for Organic Light-Emitting Diodes. *Angewandte Chemie International Edition* **2015**, *54*, 13581–13585.

(24) Hatakeyama, T.; Shiren, K.; Nakajima, K.; Nomura, S.; Nakatsuka, S.; Kinoshita, K.; Ni, J.; Ono, Y.; Ikuta, T. Ultrapure Blue Thermally Activated Delayed Fluorescence Molecules: Efficient HOMO–LUMO Separation by the Multiple Resonance Effect. *Advanced Materials* **2016**, *28*, 2777–2781.

(25) Nakatsuka, S.; Gotoh, H.; Kinoshita, K.; Yasuda, N.; Hatakeyama, T. Divergent Synthesis of Heteroatom-Centered 4,8,12-Triazatriangulenes. *Angewandte Chemie International Edition* **2017**, *56*, 5087–5090.

(26) Oda, S.; Kawakami, B.; Kawasumi, R.; Okita, R.; Hatakeyama, T. Multiple Resonance Effect-Induced Sky-Blue Thermally Activated Delayed Fluorescence with a Narrow Emission Band. *Organic Letters* **2019**, *21*, 9311–9314.

(27) Ikeda, N.; Oda, S.; Matsumoto, R.; Yoshioka, M.; Fukushima, D.; Yoshiura, K.; Yasuda, N.; Hatakeyama, T. Solution-Processable Pure Green Thermally Activated Delayed Fluorescence Emitter Based on the Multiple Resonance Effect. *Advanced Materials* **2020**, *32*.

(28) Cheng, Y.; Fan, X.; Huang, F.; Xiong, X.; Yu, J.; Wang, K.; Lee, C.; Zhang, X. A Highly Twisted Carbazole-Fused DABNA Derivative as an Orange-Red TADF Emitter for OLEDs with Nearly 40.

(29) Di Maiolo, F.; Phan Huu, D. K. A.; Giavazzi, D.; Landi, A.; Racchi, O.; Painelli, A. Shedding light on thermally-activated delayed fluorescence. *Chemical Science* **2024**, *15*, 5434–5450.

(30) Northey, T.; Penfold, T. The intersystem crossing mechanism of an ultrapure blue organoboron emitter. *Organic Electronics* **2018**, *59*, 45–48.

(31) Kim, I.; Cho, K. H.; Jeon, S. O.; Son, W.-J.; Kim, D.; Rhee, Y. M.; Jang, I.; Choi, H.; Kim, D. S. Three States Involving Vibronic Resonance is a Key to Enhancing Reverse Intersystem Crossing Dynamics of an Organoboron-Based Ultrapure Blue Emitter. *JACS Au* **2021**, *1*, 987–997.

(32) Eng, J.; Penfold, T. J. Open questions on the photophysics of thermally activated delayed fluorescence. *Communications Chemistry* **2021**, *4*.

(33) Shizu, K.; Kaji, H. Comprehensive understanding of multiple resonance thermally activated delayed fluorescence through quantum chemistry calculations. *Communications Chemistry* **2022**, *5*.

(34) Won, T.; Nakayama, K.-i.; Aizawa, N. Inverted singlet–triplet emitters for organic light-emitting diodes. *Chemical Physics Reviews* **2023**, *4*, 021310.

(35) Li, J.; Zhang, Q.; Nomura, H.; Miyazaki, H.; Adachi, C. Thermally activated delayed fluorescence from $^3n\pi^*$ to $^1n\pi^*$ up-conversion and its application to organic light-emitting diodes. *Applied Physics Letters* **2014**, *105*, 013301.

(36) Wu, X.; Su, B.-K.; Chen, D.-G.; Liu, D.; Wu, C.-C.; Huang, Z.-X.; Lin, T.-C.; Wu, C.-H.; Zhu, M.; Li, E. Y.; Hung, W.-Y.; Zhu, W.; Chou, P.-T. The role of host–guest interactions in organic emitters employing MR-TADF. *Nature Photonics* **2021**, *15*, 780–786.

(37) Jiang, H.; Cao, Y.; Yang, Q.; Xian, L.; Tao, Y.; Chen, R.; Huang, W. Organic Resonance Materials: Molecular Design, Photophysical Properties, and Optoelectronic Applications. *The Journal of Physical Chemistry Letters* **2020**, *11*, 7739–7754.

(38) Suresh, S. M.; Hall, D.; Beljonne, D.; Olivier, Y.; Zysman-Colman, E. Multiresonant Thermally Activated Delayed Fluorescence Emitters Based on Heteroatom-Doped Nanographenes: Recent Advances and Prospects for Organic Light-Emitting Diodes. *Advanced Functional Materials* **2020**, *30*, 1908677.

(39) Liu, Y.; Xiao, X.; Ran, Y.; Bin, Z.; You, J. Molecular design of thermally activated delayed fluorescent emitters for narrowband orange–red OLEDs boosted by a cyano-functionalization strategy. *Chemical Science* **2021**, *12*, 9408–9412.

(40) Wu, S.; Li, W.; Yoshida, K.; Hall, D.; Suresh, S. M.; Sayner, T.; Gong, J.; Beljonne, D.; Olivier, Y.; Samuel, I. D. W.; Zysman-Colman, E. Excited-State Modulation in Donor-Substituted Multiresonant Thermally Activated Delayed Fluorescence Emitters. *ACS Applied Materials & Interfaces* **2022**, *14*, 22341–22352.

(41) Li, J.; Li, Z.; Liu, H.; Gong, H.; Zhang, J.; Li, X.; Wang, Y.; Guo, Q. Down-conversion-induced delayed fluorescence via an inverted singlet-triplet channel. *Dyes and Pigments* **2022**, *203*, 110366.

(42) Gao, H.; Shen, S.; Qin, Y.; Liu, G.; Gao, T.; Dong, X.; Pang, Z.; Xie, X.; Wang, P.; Wang, Y. Ultrapure Blue Thermally Activated Delayed Fluorescence (TADF) Emitters Based on Rigid Sulfur/Oxygen-Bridged Triarylboron Acceptor: MR TADF and D–A TADF. *The Journal of Physical Chemistry Letters* **2022**, *13*, 7561–7567.

(43) Sano, Y.; Shintani, T.; Hayakawa, M.; Oda, S.; Kondo, M.; Matsushita, T.; Hatakeyama, T. One-Shot Construction of BN-Embedded Heptadecacene Framework Exhibiting Ultra-narrowband Green Thermally Activated Delayed Fluorescence. *Journal of the American Chemical Society* **2023**, *145*, 11504–11511.

(44) Jin, J.; Duan, C.; Jiang, H.; Tao, P.; Xu, H.; Wong, W.-Y. Integrating Asymmetric O-B-N Unit in Multi-Resonance Thermally Activated Delayed Fluorescence Emit-

ters towards High-Performance Deep-Blue Organic Light-Emitting Diodes. *Angewandte Chemie International Edition* **2023**, *62*, 18.

(45) Wu, S.; Zhang, L.; Wang, J.; Kumar Gupta, A.; Samuel, I. D. W.; Zysman-Colman, E. Merging Boron and Carbonyl based MR-TADF Emitter Designs to Achieve High Performance Pure Blue OLEDs. *Angewandte Chemie International Edition n/a*, e202305182.

(46) de Silva, P. Inverted singlet–triplet gaps and their relevance to thermally activated delayed fluorescence. *The Journal of Physical Chemistry Letters* **2019**, *10*, 5674–5679.

(47) Pershin, A.; Hall, D.; Lemaur, V.; Sancho-Garcia, J.-C.; Muccioli, L.; Zysman-Colman, E.; Beljonne, D.; Olivier, Y. Highly emissive excitons with reduced exchange energy in thermally activated delayed fluorescent molecules. *Nature Communications* **2019**, *10*, 597.

(48) Pratik, S. M.; Coropceanu, V.; Brédas, J.-L. Purely Organic Emitters for Multiresonant Thermally Activated Delay Fluorescence: Design of Highly Efficient Sulfur and Selenium Derivatives. *ACS Materials Letters* **2022**, *4*, 440–447.

(49) Pratik, S. M.; Coropceanu, V.; Brédas, J.-L. Enhancement of Thermally Activated Delayed Fluorescence (TADF) in Multi-Resonant Emitters via Control of Chalcogen Atom Embedding. *Chemistry of Materials* **2022**, *34*, 8022–8030.

(50) Drwal, D.; Matousek, M.; Golub, P.; Tucholska, A.; Hapka, M.; Brabec, J.; Veis, L.; Pernal, K. Role of Spin Polarization and Dynamic Correlation in Singlet–Triplet Gap Inversion of Heptazine Derivatives. *Journal of Chemical Theory and Computation* **2023**, *19*, 7606–7616.

(51) Loos, P.-F.; Lipparini, F.; Jacquemin, D. Heptazine, Cyclazine, and Related Compounds: Chemically-Accurate Estimates of the Inverted Singlet–Triplet Gap. *The Journal of Physical Chemistry Letters* **2023**, *14*, 11069–11075.

(52) Pariser, R.; Parr, R. G. A Semi-Empirical Theory of the Electronic Spectra and Electronic Structure of Complex Unsaturated Molecules. I. *The Journal of Chemical Physics* **1953**, *21*, 466–471.

(53) Pariser, R.; Parr, R. G. A Semi-Empirical Theory of the Electronic Spectra and Electronic Structure of Complex Unsaturated Molecules. II. *The Journal of Chemical Physics* **1953**, *21*, 767–776.

(54) Pople, J. A. Electron interaction in unsaturated hydrocarbons. *Transactions of the Faraday Society* **1953**, *49*, 1375.

(55) Pariser, R. Theory of the Electronic Spectra and Structure of the Polyacenes and of Alternant Hydrocarbons. *The Journal of Chemical Physics* **1956**, *24*, 250–268.

(56) Pariser, R. Electronic Spectrum and Structure of Azulene. *The Journal of Chemical Physics* **1956**, *25*, 1112–1116.

(57) Favini, G.; Vandoni, I.; Simonetta, M. Calculation of electronic spectra of aza-benzenes and aza-naphthalenes by the Pariser-Parr-Pople method. *Theoretica Chimica Acta* **1965**, *3*, 45–58.

(58) Albert, I. D. L.; Ramasesha, S.; Das, P. K. Properties of some low-lying electronic states in polymethineimines and poly(2,3-diazabutadienes). *Physical Review B* **1991**, *43*, 7013–7019.

(59) Mukhopadhyay, S.; Topham, B. J.; Soos, Z. G.; Ramasesha, S. Neutral and Charged Excited States in Polar Organic Films: Origin of Unusual Electroluminescence in Tri-*p*-tolylamine-Based Hole Conductors. *The Journal of Physical Chemistry A* **2008**, *112*, 7271–7279.

(60) Kumar, M.; Pati, Y. A.; Ramasesha, S. A density matrix renormalization group method

study of optical properties of porphines and metalloporphines. *The Journal of Chemical Physics* **2012**, *136*, 014112.

(61) Thomas, S.; Pati, Y.; Ramasesha, S. Linear and nonlinear optical properties of expanded porphyrins: A DMRG study. *The Journal of Physical Chemistry A* **2013**, *117*, 7804–7809.

(62) Aryanpour, K.; Shukla, A.; Mazumdar, S. Electron correlations and two-photon states in polycyclic aromatic hydrocarbon molecules: A peculiar role of geometry. *The Journal of Chemical Physics* **2014**, *140*, 104301.

(63) Bhattacharyya, P.; Rai, D. K.; Shukla, A. Pariser–Parr–Pople Model Based Configuration-Interaction Study of Linear Optical Absorption in Lower-Symmetry Polycyclic Aromatic Hydrocarbon Molecules. *The Journal of Physical Chemistry C* **2020**, *124*, 14297–14305.

(64) Poh, Y. R.; Morozov, D.; Kazmierczak, N. P.; Hadt, R. G.; Groenhof, G.; Yuen-Zhou, J. Alternant Hydrocarbon Diradicals as Optically Addressable Molecular Qubits. *Journal of the American Chemical Society* **2024**,

(65) Misurkin, I. A.; Ovchinnikov, A. A. The Electronic Structure of Conjugated Systems in Terms of the Pariser–Parr–Pole Approximation. *Russian Chemical Reviews* **1974**, *43*, 1072.

(66) Ohno, K. Some remarks on the Pariser-Parr-Pople method. *Theoretica chimica acta* **1964**, *2*, 219–227.

(67) Lehoucq, R.; Sorensen, D.; Yang, C. *ARPACK Users' Guide*; Society for Industrial and Applied Mathematics, 1998.

(68) Sandoval-Salinas, M. E.; Carreras, A.; Casanova, D. Triangular graphene nanofrag-

ments: open-shell character and doping. *Physical Chemistry Chemical Physics* **2019**, *21*, 9069–9076.

(69) Casanova, D. Restricted active space configuration interaction methods for strong correlation: Recent developments. *WIREs Computational Molecular Science* **2021**, *12*.

(70) Casanova, D.; Head-Gordon, M. Restricted active space spin-flip configuration interaction approach: theory, implementation and examples. *Physical Chemistry Chemical Physics* **2009**, *11*, 9779.

(71) Pios, S.; Huang, X.; Sobolewski, A. L.; Domcke, W. Triangular boron carbon nitrides: An unexplored family of chromophores with unique properties for photocatalysis and optoelectronics. *Physical Chemistry Chemical Physics* **2021**, *23*, 12968–12975.

(72) Soos, Z. G.; Ramasesha, S. Valence-bond theory of linear Hubbard and Pariser-Parr-Pople models. *Physical Review B* **1984**, *29*, 5410–5422.

(73) Prodhan, S.; Soos, Z. G.; Ramasesha, S. Model for triplet state engineering in organic light emitting diodes. *The Journal of Chemical Physics* **2014**, *140*, 214313.

(74) Nishimoto, K.; Forster, L. S. SCFMO calculations of heteroatomic systems with the variable? approximation. *Theoretica Chimica Acta* **1966**, *4*, 155–165.

(75) Michl, J.; Koutecky, J.; Becker, R. S.; Earhart, C. E. A note on the parameters for heteroatoms in Pariser-Parr-Pople (PPP) calculations. *Theoretica Chimica Acta* **1970**, *19*, 92–97.

(76) Hinze, J.; Beveridge, D. L. Parametrization of semiempirical π-electron molecular orbital calculations. π Systems containing carbon, nitrogen, oxygen, and fluorine. *Journal of the American Chemical Society* **1971**, *93*, 3107–3114.

(77) Zahradník, R.; Tesařová, I.; Pancíř, J. Experimental and theoretical (HMO and LCI-SCF) study of singlet-triplet transitions in conjugated hydrocarbons and their derivatives. *Collection of Czechoslovak Chemical Communications* **1971**, *36*, 2867–2880.

(78) Griffiths, J. Practical aspects of colour prediction of organic dye molecules. *Dyes and Pigments* **1982**, *3*, 211–233.

(79) Grossjean, M. F.; Tavan, P. Wavelength regulation in bacteriorhodopsin and halorhodopsin: A Pariser–Parr–Pople multireference double excitation configuration interaction study of retinal dyes. *The Journal of Chemical Physics* **1988**, *88*, 4884–4896.

(80) Albert, I. D. L.; Das, P. K.; Ramasesha, S. Optical nonlinearities in symmetric cyanine dyes and related systems. *Journal of the Optical Society of America B* **1993**, *10*, 1365.

(81) Chalvet, O.; Daudel, R.; Kaufman, J. J. LCAO-MO Calculations on Boron Compounds. I. LCAO-MO-SCF Calculations on Borazines. *Journal of the American Chemical Society* **1965**, *87*, 399–404.

(82) Armstrong, D. R.; Perkins, P. G. The electronic structure of the diphenylboron cation and the 9-borafluorenes. *Journal of the Chemical Society A: Inorganic, Physical, Theoretical* **1966**, 1026.

(83) Perkins, P. G.; Wall, D. H. Self-consistent molecular-orbital calculations on borazines. *Journal of the Chemical Society A: Inorganic, Physical, Theoretical* **1966**, 235.

(84) Baird, N. C.; Whitehead, M. A. Molecular orbital calculations for conjugated molecules containing boron and nitrogen. *Canadian Journal of Chemistry* **1967**, *45*, 2059–2070.

(85) Michl, J. Borazaro analogues of aromatic hydrocarbons. II. Semiempirical calculations. *Collection of Czechoslovak Chemical Communications* **1971**, *36*, 1248–1278.

(86) Van-Catledge, F. A. A Pariser-Parr-Pople-based set of Huckel molecular orbital parameters. *The Journal of Organic Chemistry* **1980**, *45*, 4801–4802.

(87) Radovic, L. R.; Karra, M.; Skokova, K.; Thrower, P. A. The role of substitutional boron in carbon oxidation. *Carbon* **1998**, *36*, 1841–1854.

(88) Dreuw, A.; Wormit, M. The algebraic diagrammatic construction scheme for the polarization propagator for the calculation of excited states. *WIREs Computational Molecular Science* **2014**, *5*, 82–95.

(89) Loos, P.-F.; Lipparini, F.; Boggio-Pasqua, M.; Scemama, A.; Jacquemin, D. A Mountaineering Strategy to Excited States: Highly Accurate Energies and Benchmarks for Medium Sized Molecules. *Journal of Chemical Theory and Computation* **2020**, *16*, 1711–1741.